Monthly Notices of the ROYAL ASTRONOMICAL SOCIETY

MNRAS **00,** 1–18 (2023)
Advance Access publication 2023 June 20

https://doi.org/10.1093/mnras/stad1807

Long-term forcing of the Sun's coronal field, open flux, and cosmic ray modulation potential during grand minima, maxima, and regular activity phases by the solar dynamo mechanism

Soumyaranjan Dash [1], Dibyendu Nandy [1,2]★ and Ilya Usoskin [3]

[1] *Center of Excellence in Space Sciences India, Indian Institute of Science Education and Research Kolkata, Mohanpur 741246, West Bengal, India*
[2] *Department of Physical Sciences, Indian Institute of Science Education and Research Kolkata, Mohanpur 741246, West Bengal, India*
[3] *Space Physics and Astronomy Research Unit and Sodankyla Geophysical Observatory, University of Oulu, 90014, Finland*

Accepted 2023 June 13. Received 2023 June 10; in original form 2022 September 7

ABSTRACT

Magnetic fields generated in the Sun's interior by the dynamo mechanism drive solar activity over a range of time-scales. Direct sunspot observations exist for a few centuries; reconstructed variations based on cosmogenic isotopes in the solar open flux and cosmic ray flux exist over thousands of years. While such reconstructions indicate the presence of extreme solar activity fluctuations in the past, causal links between millennia scale dynamo activity, consequent coronal field, solar wind, open flux and cosmic ray flux variations remain elusive; a lack of coronal field observations compounds this issue. By utilizing a stochastically forced solar dynamo model and potential field source surface extrapolation, we perform long-term simulations to illuminate how dynamo generated magnetic fields govern the structure of the solar corona and the state of the heliosphere – as indicated by variations in the open flux and cosmic ray modulation potential. We establish differences in the nature of the large-scale structuring of the solar corona during grand maximum, minimum, and regular solar activity phases and simulate how the open flux and cosmic ray modulation potential vary across these different phases of activity. We demonstrate that the power spectrum of simulated and observationally reconstructed solar open flux time series are consistent with each other. Our study provides the theoretical foundation for interpreting long-term solar cycle variations inferred from cosmogenic isotope based reconstructions and establishes causality between solar internal variations to the forcing of the state of the heliosphere.

Key words: Sun: activity – Sun: corona – Sun: heliosphere – Sun: magnetic fields – dynamo.

1 INTRODUCTION

The variability of solar magnetic activity over long time scales is manifested in multiple observable proxies. Direct solar observations for the past ∼400 yr have revealed significant variability in the solar magnetic cycle, covering a period of extremely low activity known as the Maunder minimum (second half of the 17th century, Eddy 1988) to a period of increased activity known as the Modern grand maximum (middle of the 20th century Solanki et al. 2004). Modulations in solar cycle amplitude and duration are indicators of such fluctuations. The impact of solar magnetic fields on the state of the heliosphere – as it emerges through the surface, evolves, and extends into the solar corona – is manifested via the open solar flux (here after OSF). It is the distribution of the coronal magnetic fields that determines the solar open flux. The magnetic activity evolution of the Sun and other stars directly influences the environment of the harboured planets (Nandy 2004; Nandy & Martens 2007; Bharati Das et al. 2019). Our current understanding of the long-term solar variability and its impact on Solar system planets with observations, reconstructions, and theoretical modelling has improved over the years (Nandy et al. 2021). However, the causal link between millennia-scale solar dynamo activity and the consequent variations in the state of the heliosphere via coronal magnetic field dynamics remains unexplored.

Multimillennial reconstructions of solar activity based on cosmogenic isotopes such as ^{10}Be (in polar ice cores) and ^{14}C (in tree rings) show the presence of grand minima, maxima, and regular activity phases (Usoskin et al. 2003; Solanki et al. 2004; Usoskin 2017; Wu et al. 2018). The flux of galactic cosmic rays near the Earth is modulated by variations in the heliospheric magnetic field, which is a result of solar magnetic activity governed by the solar dynamo mechanism. Fluctuations in the cosmic ray flux provide critical insights towards understanding solar activity variations (Owens, Usoskin & Lockwood 2012). One of the critical questions in this regard is whether grand minima and maxima episodes are the outcome of special states of the solar dynamo mechanism or if they result from random variability (Carbonell, Oliver & Ballester 1994; Nandy, Muñoz-Jaramillo & Martens 2011; Choudhuri & Karak 2012; Tripathi, Nandy & Banerjee 2021). Direct observations of the emergence of sunspots on the solar surface, which only exists from the early 17th century onwards, are not sufficient to definitively constrain such extreme episodes. Long-term solar dynamo simulations that generate such variations hold the key to explain the evolution of the solar coronal magnetic field configuration that modulates the heliospheric parameters, e.g. open flux, solar wind, and cosmic ray modulation potential.

★ E-mail: dnandi@iiserkol.ac.in

Long-term solar dynamo simulations with stochastic fluctuations in the poloidal-field source can generate extreme fluctuations with grand maximum and minimum-like episodes (Hazra, Passos & Nandy 2014; Passos et al. 2014; Albert et al. 2021). The Babcock–Leighton mechanism for poloidal field generation in dynamo models of the solar cycle appears to be quite successful in explaining various manifestations of solar magnetism (Nandy & Choudhuri 2002; Jouve et al. 2008; Dasi-Espuig et al. 2010; Nandy et al. 2011; Cameron & Schüssler 2015; Charbonneau 2020). Solar dynamo models can explain these different modes of solar activity fluctuation (Tripathi et al. 2021) and are widely used in solar cycle prediction studies (Bhowmik & Nandy 2018; Nandy 2021). Magnetic fields generated in the solar interior via the solar dynamo mechanism emerge on the surface and govern the structuring and evolution of the corona. The distribution of the large-scale coronal magnetic fields that expand into the heliosphere facilitates the flow of solar wind plasma into the interplanetary medium and impacts the propagation of cosmic ray particles. Unlike sunspots, it is difficult to observe solar coronal magnetic fields directly due to low coronal plasma density and a bright photospheric background. Hence, we rely on data-driven modelling approaches to constrain the coronal fields. The evolution of OSF derived from coronal magnetic fields is an indicator of the solar forcing on the heliosphere. Past studies by Schatten, Wilcox & Ness (1969); Hoeksema, Wilcox & Scherrer (1983); Schrijver & De Rosa (2003); Yeates et al. (2010); Lee et al. (2011) show the evolution of the OSF over solar cycle time-scales.

Potential field source surface extrapolation (PFSS) is one of the widely used approaches to modelling the global coronal magnetic fields using photospheric magnetic field distribution as an input (Altschuler & Newkirk 1969; Schatten et al. 1969; Schrijver & De Rosa 2003). Assuming a vanishing current density, the PFSS model provides a unique magnetic field solution in a region between the surface at $r = R_\odot$ and a spherically symmetric source surface at $r = R_{SS}$, where the magnetic fields are assumed to become purely radial. The unsigned magnetic flux through the source surface (R_{SS}) is defined as the OSF. The source surface height is typically set to $R_{SS} = 2.5\,R_\odot$ based on a comparison of PFSS models and observed coronal structures (Schatten et al. 1969; Hoeksema et al. 1983). However, the source surface is believed to vary with solar magnetic activity levels. During solar minimum phases, the source surface moves closer to the surface (Lee et al. 2011). There exist multiple studies, wherein, the height of the source surface is adjusted in order to minimize the misfit between the modelled and observed OSF at different phases of solar activity cycle. Earlier studies show a source surface height ranging from 1.8–2.5 $R_\odot$ provides a reasonable agreement between the modelled and observed OSF (Lee et al. 2011; Arden, Norton & Sun 2014; Badman et al. 2020; Réville et al. 2020). A comparison between the PFSS-generated magnetic field and the observations of the interplanetary magnetic field provides an idea of the possible source surface height. Predictive approaches with the coupled surface flux transport model and the PFSS extrapolation have shown great potential for reasonably accurate prediction of large-scale coronal magnetic field configurations (Nandy et al. 2018; Dash et al. 2020). In order to understand the coronal structure during a grand minimum phase, Riley et al. (2015) modelled coronal magnetic fields using global magnetohydrodynamic simulations. Global solar coronal configuration for past eclipses during grand minimum episodes is also explored by Hayakawa et al. (2020, 2021); Lockwood & Owens (2021) using historic paintings.

Coronal magnetic field structure and its evolution modulate the state of the heliosphere, which is reflected in the cosmic ray flux on the Earth. The modulation of cosmic rays due to solar activity is parametrized by the force-field approximation via the so-called modulation potential (e.g, Usoskin et al. 2005). Using cosmogenic-isotope ^{14}C measurements found in tree rings, the solar forcing on the cosmic rays is measured in terms of OSF and a reconstructed sunspot number time series. Usoskin et al. (2021) reconstructed the OSF for the past ∼1000 years with an annual cadence utilizing the cosmic ray flux assessed from cosmogenic-isotope ^{14}C measurements in tree rings (Brehm et al. 2021). Apart from cosmic ray flux, *in situ* magnetic field observations are also used to infer the evolution of OSF for past solar cycles (Lockwood & Owens 2014). Long-term variations in OSF explain the variations in the state of the heliosphere due to solar forcing of coronal magnetic fields (Owens & Forsyth 2013; Krivova et al. 2021). It is important to note that OSF is a spatially averaged quantity and hence lacks information about the large-scale coronal magnetic field structuring. Therefore modelling of coronal structures can provide critical insights to explain the solar forcing on these globally averaged quantities, e.g. OSF and cosmic ray modulation potential.

In this study, we explore the coronal magnetic field configuration during regular activity, grand maximum, and grand minimum phases. Our aim is to explore causal connections between the reconstructed solar activity and different phases of the solar dynamo by coupling the solar dynamo simulations to a PFSS model. We demonstrate differences in the nature of the coronal magnetic field configuration during these phases and discuss the resulting impacts on heliospheric parameters. Numerical model set-ups are explained in Section 2. We present our results explaining the variations in magnetic field strength, coronal magnetic field configuration, OSF, and cosmic ray modulation potential for different solar activity episodes in Section 3. Finally, we conclude with a summary in Section 4.

2 THEORETICAL MODELLING

2.1 Solar dynamo model

We simulate the Babcock–Leighton (BL) dynamo model (Babcock 1961; Leighton 1969) with imposed stochastic fluctuations on the poloidal source. We utilize the 2.5D axisymmetric solar dynamo model – `SURYA`, which works in a kinematic regime (Nandy & Choudhuri 2001, 2002; Chatterjee, Nandy & Choudhuri 2004). The global magnetic field of the Sun can be expressed as a combination of poloidal and toroidal components in spherical polar coordinates i.e.

$$\mathbf{B} = B(r,\theta,t)\mathbf{e}_\phi + \mathbf{B_p}, \tag{1}$$

where $\mathbf{B_p} = \nabla \times [A(r,\theta,t)\mathbf{e}_\phi]$ corresponds to the poloidal component, and $B(r,\theta,t)\mathbf{e}_\phi$ denotes the toroidal component, at any time instant t. The dynamo equations are obtained by solving the magnetic induction equation for $\mathbf{B}$, which can be written as,

$$\frac{\partial A}{\partial t} + \frac{1}{s}[\mathbf{v_p}\cdot\nabla(sA)] = \eta_p\left(\nabla^2 - \frac{1}{s^2}\right)A + (\alpha_{MF} + \alpha_{BL})B, \tag{2}$$

$$\frac{\partial B}{\partial t} + s\left[\mathbf{v_p}\cdot\nabla\left(\frac{B}{s}\right)\right] + (\nabla\cdot\mathbf{v_p})B = \eta_t\left(\nabla^2 - \frac{1}{s^2}\right)B + s(\mathbf{B_p}\cdot\nabla\Omega) + \frac{1}{s}\frac{\partial(sB)}{\partial r}\frac{\partial\eta_t}{\partial r}, \tag{3}$$

where, $s = r\sin(\theta)$. Equations (2) and (3) are solved on a uniform 129 × 129 grid between $0.55R_\odot < r < R_\odot$ and $0 < \theta < \pi$. The poloidal field source term imbibes both the BL mechanism (α_{BL}) and mean-field α-effect (α_{MF}).

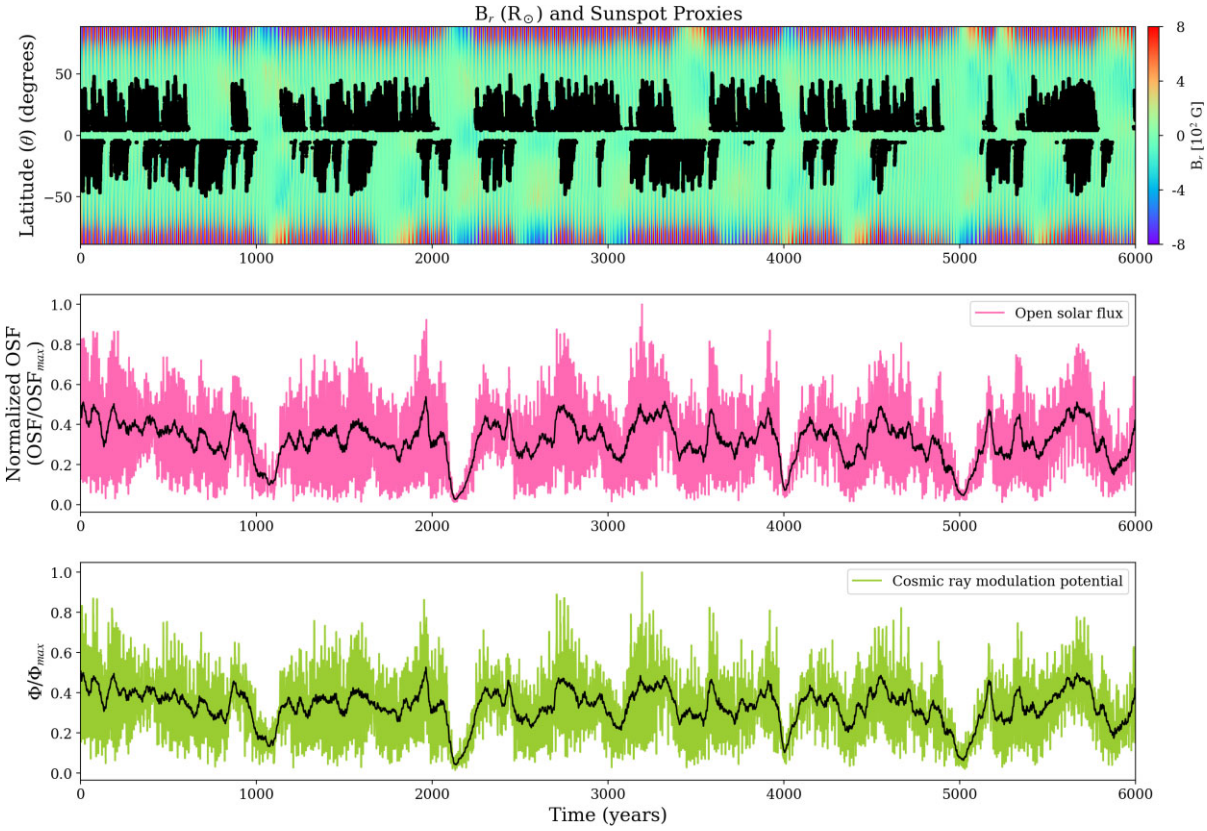

Figure 1. Long-term stochastically forced solar dynamo simulation for 6000 years. The top panel shows a butterfly diagram of the surface radial magnetic field (B_r). The emergence latitudes of the sunspot eruption proxies are overplotted in black. The middle panel denotes normalized OSF computed using solar dynamo simulation and the PFSS model in the magenta curve. A 22-year running average of the modelled OSF time series is plotted in the solid black curve. In the lower panel, we plot the modelled normalized cosmic ray modulation potential in solid green colour and the corresponding 22-year running average in solid black. For the grand minimum phase, sunspot eruption proxies are absent on the solar surface. Hence, the resulting heliospheric modulation due to solar activity variation, which is indicated by the OSF and the cosmic ray modulation potential show a drop in magnitude for these phases. Similarly, we find signatures of enhanced OSF and cosmic ray modulation potential corresponding to grand maximum phases (periods of higher solar activity) in our modelled output.

The meridional circulation which advects and distorts the magnetic field in each hemisphere is modelled through a single cell flow represented by $\mathbf{v_p}$ and $\Omega(r,\,\theta)$ denotes the differential rotation in the solar convection zone (SCZ). In our model, we assume different magnetic diffusivities for the poloidal and toroidal field components, namely η_p and η_t, respectively. The SURYA dynamo code uses different diffusivity terms for toroidal and poloidal field components to model the effect of suppression of turbulence by the relatively stronger toroidal component of the magnetic field (see e.g. Muñoz-Jaramillo et al. 2010). The value for the η_p and η_t are set to be 2.6×10^{12} and $4.0 \times 10^{10}\,\mathrm{cm^2\,s^{-1}}$, respectively. Specifically, our model is adapted from Passos et al. (2014), which introduced stochastic fluctuations and an additional mean-field α-effect for recovery of cycles from grand minima episodes. The mean-field α-effect is distributed through the bulk of the solar convection zone and is quenched by fields exceeding 10^4 G, whereas the BL α-source ($\alpha_{\rm BL}$) operates near the surface. For further details refer to Passos et al. (2014). The presence of both the BL poloidal source and mean-field α-effect add interesting aspects to the dynamics of the solar cycle as recently explored in the context of solar cycle predictability (Hazra, Brun & Nandy 2020).

The idea behind introducing stochasticity in the BL α-source ($\alpha_{\rm BL}$) is to mimic the modulation in the surface BL mechanism by scatter (around the mean Joy's law) in tilt angle of emerged bipolar sunspot pairs. Likewise, fluctuations in the mean-field α-source ($\alpha_{\rm MF}$) dictate the impact of turbulent helical convection in the deep interior. The combined action of the poloidal source terms facilitates recovery from grand minimum (Hazra et al. 2014; Passos et al. 2014). The BL α-effect is defined by:

$$\alpha_{\rm BL}(r,\theta) = \alpha_{\rm BL}^0 \frac{\cos\theta}{4}\left[1+\mathrm{erf}\left(\frac{r-r_1}{d_1}\right)\right]\times\left[1-\mathrm{erf}\left(\frac{r-r_2}{d_2}\right)\right] \times a_1\left[1+\mathrm{erf}\left(\frac{B_\phi^2-B_{1lo}^2}{d_3^2}\right)\right]\times\left[1-\mathrm{erf}\left(\frac{B_\phi^2-B_{1\,\rm up}^2}{d_4^2}\right)\right]. \quad (4)$$

Upper and lower quenching terms $B_{1\,\rm up}$, $B_{1\,\rm lo}$ are introduced in equation (4). Such parametrization of the $\alpha_{\rm BL}$ is important from a physical perspective. On the one hand, toroidal fields, which are very weak, do not coherently emerge to produce bipolar sunspot pairs and thus cannot contribute to poloidal field generation. On the other hand, very strong toroidal fields which do not pick up significant tilt do not produce significant polar fields. The values of the constants are set to $r_1 = 0.95R_\odot$, $r_2 = R_\odot$, and $d_1 = d_2 = 0.025R_\odot$. The $\alpha_{\rm BL}^0 = 27\,\mathrm{m\,s^{-1}}$ controls the amplitude of the source term; $a_1 = 0.393$ is a normalization constant; the lower threshold $B_{1\,\rm lo} = 10^3$ G; $d_3 = 10^2$ G; the upper threshold $B_{1\,\rm up} = 5 \times 10^5$ G and $d_4 = 10^6$ G. The detail description of the quantities mentioned in equation (4) and their mathematical parametrization, are available in Passos et al. (2014).

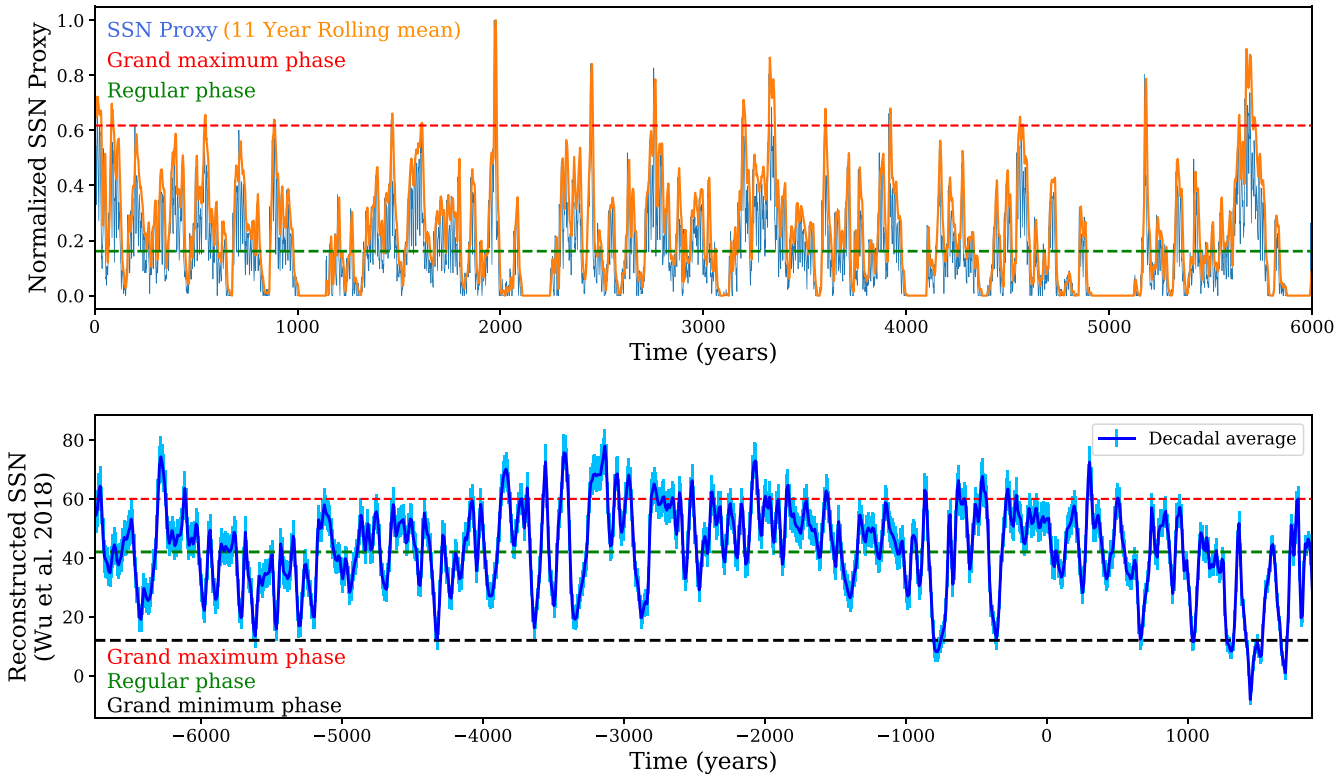

Figure 2. Sunspot number time series. Normalized time series of solar dynamo generated sunspot eruption proxy for 6000 years is shown in blue in the top panel. The 11-year running average of the SSN is plotted in orange. The mean sunspot number is plotted on the green-dashed curve. Episodes where the number of sunspots is greater than mean+3σ (shown in the red-dashed curve), are identified as grand maxima. Phases with no sunspot eruption proxies are the grand minimum phases in our simulation. In the bottom panel, reconstructed decadal averaged SSN (Wu et al. 2018) is shown in the blue curve. Here, the minimum threshold for the grand maximum phases is denoted by the red-dashed curve. The green-dashed curve shows the main component (normal/moderate phase), and the black-dashed line denotes the grand minimum component of the reconstructed solar activity cycle. There are multiple grand maxima and grand minima phases present in both the reconstructed time series and our long-term solar dynamo simulation.

The dispersion in the poloidal source term distribution controls the poloidal field amplitude and thus the solar cycle strength. Random stochastic fluctuations of strength 150 per cent are introduced around the mean value of the $\alpha_{\rm BL}$, denoted by $\alpha^0_{\rm BL}$, so that $\alpha_{\rm BL} = \alpha^0_{\rm BL} + \alpha^{\rm fluc}_{\rm BL}\,\sigma(t,\tau)$. Here, $\alpha^0_{\rm BL}$ is set to 27 m s^{-1} and $\sigma(t,\tau)$ is assigned random values between $[-1.5, 1.5]$ after each coherence time τ (here 6 months). $\alpha^{\rm fluc}_{\rm BL}$ is set to the same value as $\alpha^0_{\rm BL}$.

For the buoyancy algorithm, our model searches for toroidal field exceeding a critical threshold ($B_{\rm c} = 8 \times 10^4$ G) at the base of the convection zone (at $r = 0.71 R_\odot$). When this condition is satisfied, the algorithm removes half of the toroidal field and deposits this field near the surface, where the near-surface α-effect acts locally on the toroidal field to mimic the BL mechanism. The eruptions are proxies for sunspots in our simulation set-up and their latitude and time of emergence are used to reconstruct the simulated butterfly diagrams (Nandy & Choudhuri 2001, 2002; Chatterjee et al. 2004).

The number of sunspot eruption proxies is counted using the aforementioned buoyancy algorithm to model the sunspot proxy time series. We also calculate the surface radial magnetic field using the magnetic vector potential A using the following expression:

$$B_r = \frac{1}{R\sin\theta}\left[\frac{\partial(A\sin\theta)}{\partial\theta}\right]. \quad (5)$$

We performed a 6000-year-long solar dynamo simulation. However, our dynamo simulation is not calibrated to observations and hence is not suitable for direct comparison with observed quantities. In this paper, we intend to understand the qualitative nature of the magnetic field evolution during grand maxima, grand minima, and regular activity phases.

2.2 Solar coronal magnetic field model

Reconstruction of large-scale coronal magnetic fields can be done following the PFSS technique (Altschuler & Newkirk 1969; Schatten et al. 1969) utilizing the surface radial magnetic field as a lower boundary condition. This technique assumes the solar corona to be current-free till a spherical source surface (of radius $r = R_{\rm ss}$). Beyond the source surface, the impact of solar wind is dominant which makes the magnetic field lines purely radial. Hence in the region $R_\odot \le r \le R_{\rm ss}$,

$$\nabla \times \mathbf{B} = 0. \quad (6)$$

We can express the magnetic field in terms of a scalar potential ϕ that satisfies,

$$-\nabla\phi = \mathbf{B}. \quad (7)$$

Since $\nabla \cdot \mathbf{B} = 0$ we can write,

$$\nabla^2\phi = 0. \quad (8)$$

By solving for the scalar potential (ϕ), we can compute the solar coronal magnetic fields within the source surface. We use the radial magnetic field at the surface computed by the solar dynamo model

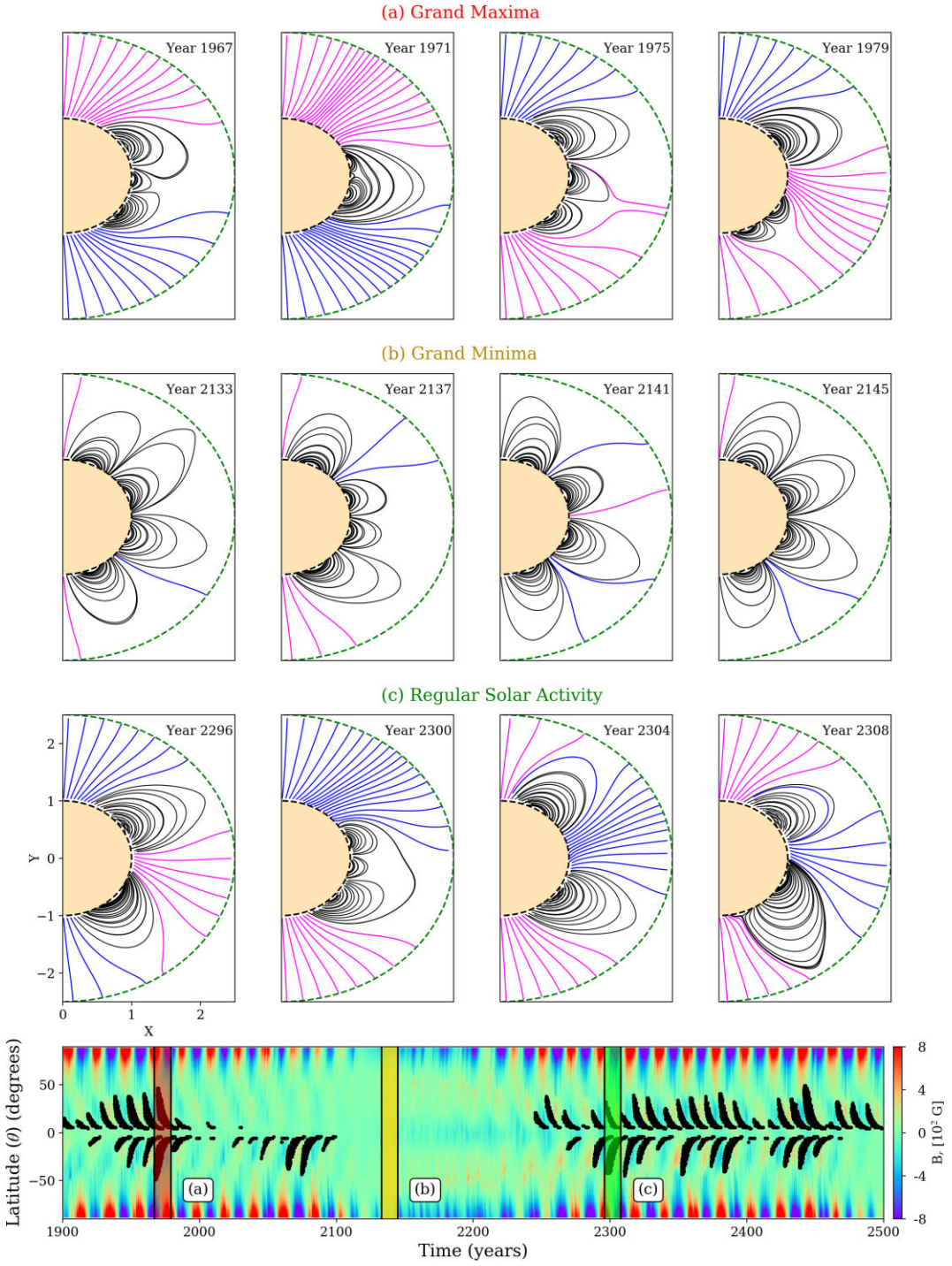

Figure 3. Evolution of solar coronal magnetic field configuration during grand maxima, grand minima, and regular solar activity phase. In the bottom panel, the surface radial magnetic field butterfly diagram is shown and the sunspot eruption proxies are plotted in black colour. Shaded regions on the butterfly diagram denote the grand maxima (red), grand minima (yellow), and regular solar activity (green) phases in the long-term solar dynamo simulation. They are labelled as (a), (b), and (c), respectively. For each of these phases, we show the corresponding coronal magnetic field configuration starting from the cycle minimum (T0) in four increments, e.g. for the grand minimum episode distribution of coronal magnetic field for the year 2133, 2137, 2141, 2145 is shown, where year 2133 and 2145 correspond to the cycle minimum. Extrapolated coronal magnetic field lines are shown, with open field lines denoted by blue (radially outward) and magenta (radially inward) curves. Closed magnetic field lines are plotted in black. A complex coronal configuration consisting of closed magnetic field lines reaching close to high-latitude regions is observed during the modelled grand minimum phase. We have fixed the source surface height at $r = 2.5R_{\odot}$ for all the phases to maintain consistency. The source surface ($r = 2.5R_{\odot}$) is denoted in the green-dashed line for all the cases. A detailed analysis of the coronal magnetic field configuration for different epochs is provided in the text.

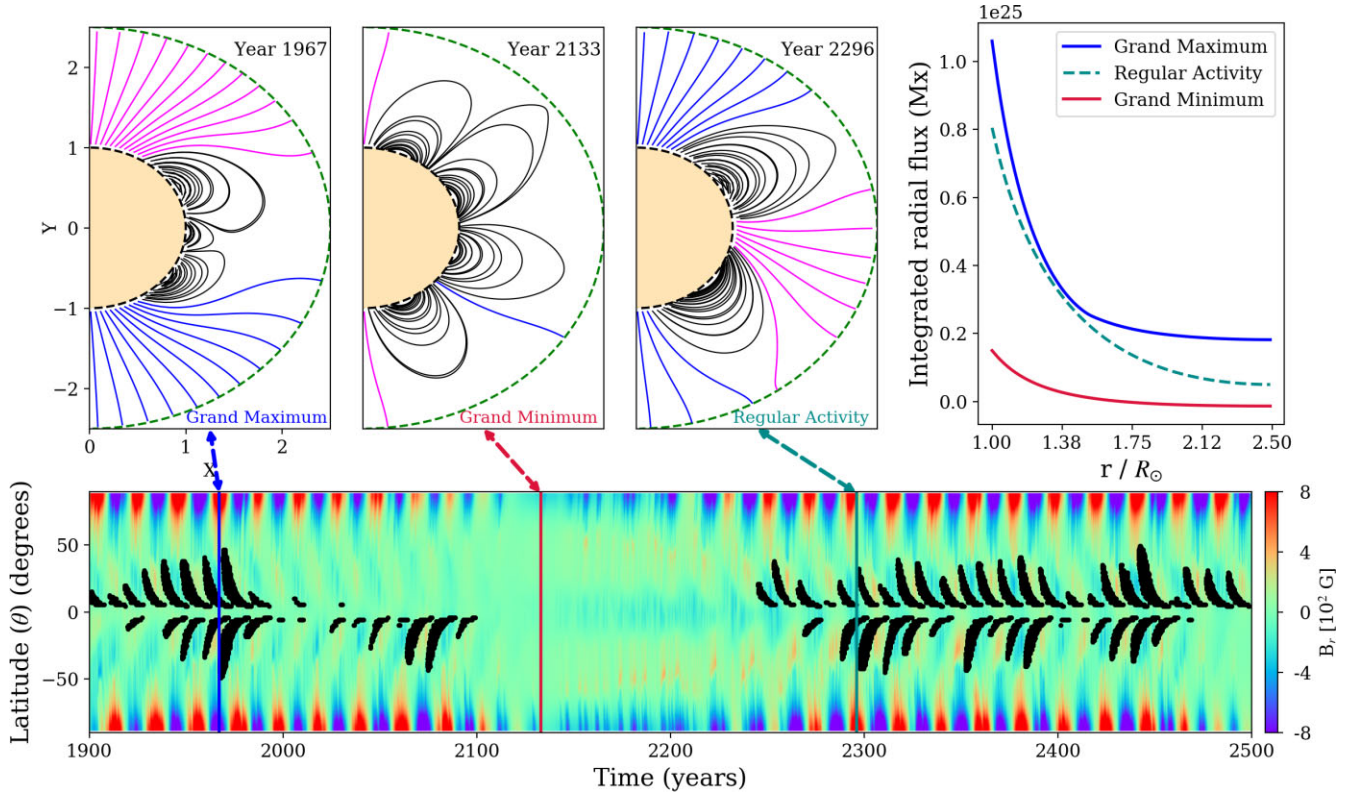

Figure 4. Reduction in magnetic field strength for different phases of solar activity. In our analysis, year 1967 corresponds to a grand maxima phase. Similarly, year 2133 and 2296 denote grand minimum and regular solar activity phase. The integrated unsigned radial flux ($\int |B_r| 2\pi r^2 \sin\theta \, d\theta$) across different radial heights are plotted in the top-right-hand panel in blue (grand maxima), dashed dark cyan (regular activity), and red (grand minimum). The decrease of over all flux from grand maxima to grand minima is observed for these three cases. In coronal magnetic field, configuration plots source surface ($r = 2.5R_\odot$) is denoted by green-dashed line. Distribution of closed and open magnetic fields for different phases (grand maximum, grand minimum, and regular) is provided with radially outward/inward open field lines plotted in blue/magenta. On the butterfly diagram (in the bottom panel), these phases are marked in solid lines for ease of understanding.

as the lower boundary condition of the PFSS model. This coronal magnetic field modelling technique is widely used in the solar physics community to compute the large-scale configuration of the corona. For a detailed derivation of the model equations, refer to Schrijver & De Rosa (2003). OSF is calculated by integrating the unsigned radial magnetic field over the source surface.

2.3 Cosmic ray modulation potential

The cosmic ray modulation potential describes the mean deceleration (i.e. loss of energy/rigidity) of galactic cosmic ray particles within the heliosphere modulated by solar activity. The process of the heliospheric cosmic ray modulation is complex (Potgieter 2013) but is often parametrized via heliospheric parameters such as OSF and the cosmic ray modulation potential (e.g. Usoskin et al. 2002; Wu et al. 2018). Solar forcing on the cosmic ray modulation (parametrized as the heliospheric modulation potential) is mediated via the OSF. We calculate cosmic ray modulation potential (Φ) using a semi-empirical formalism given by Asvestari & Usoskin (2016),

$$\Phi = \Phi_0 \times F^{n-\frac{\theta'}{\theta'_0}}(1 - \beta p). \quad (9)$$

Here, Φ and F denote the cosmic ray modulation potential and OSF, respectively. The heliospheric tilt angle (θ') denotes the average angle between the heliospheric current sheet and the equatorial plane. In our model, θ' is the angle subtended by the line joining the Sun's centre and the source surface neutral line (i.e. where $B_r = 0$ G) with respect to the solar equator. The free parameters Φ_0, θ'_0, n, and β are adopted from Asvestari & Usoskin (2016) as: $\Phi_0 = 1473.9$ MV, $\theta'_0 = 150^\circ$, $n = 1.03$, and $\beta = 0.095$. The polarity of the solar magnetic field (p) is assigned a value $p = +1$ (positive)/-1 (negative) depending on the sign of the polar fields (for our calculations, we consider the sign of the solar north pole as reference). The OSF (F) is calculated at the source surface $R_{ss} = 2.5R_\odot$ and normalized with the maximum value. This normalized OSF is used to compute the cosmic ray modulation potential.

In our 6000-year simulation, the normalization factor for the OSF is 1.8×10^{24} Mx. Using the OSF, we compute the cosmic ray modulation potential for 6000-year dynamo simulation.

3 RESULTS

In our long-term solar dynamo simulation, we find random occurrences of fluctuating solar activity phases – ranging from grand maxima to grand minima. Solar activity fluctuations can be broadly divided into two classes namely grand minima phase and regular activity phase (Usoskin et al. 2016; Wu et al. 2018). The regular activity phase includes grand maximum like the enhanced magnetic activity period and the moderate activity phases. Likewise, the periods where the solar magnetic activity level is minimum are categorized as grand minima phases.

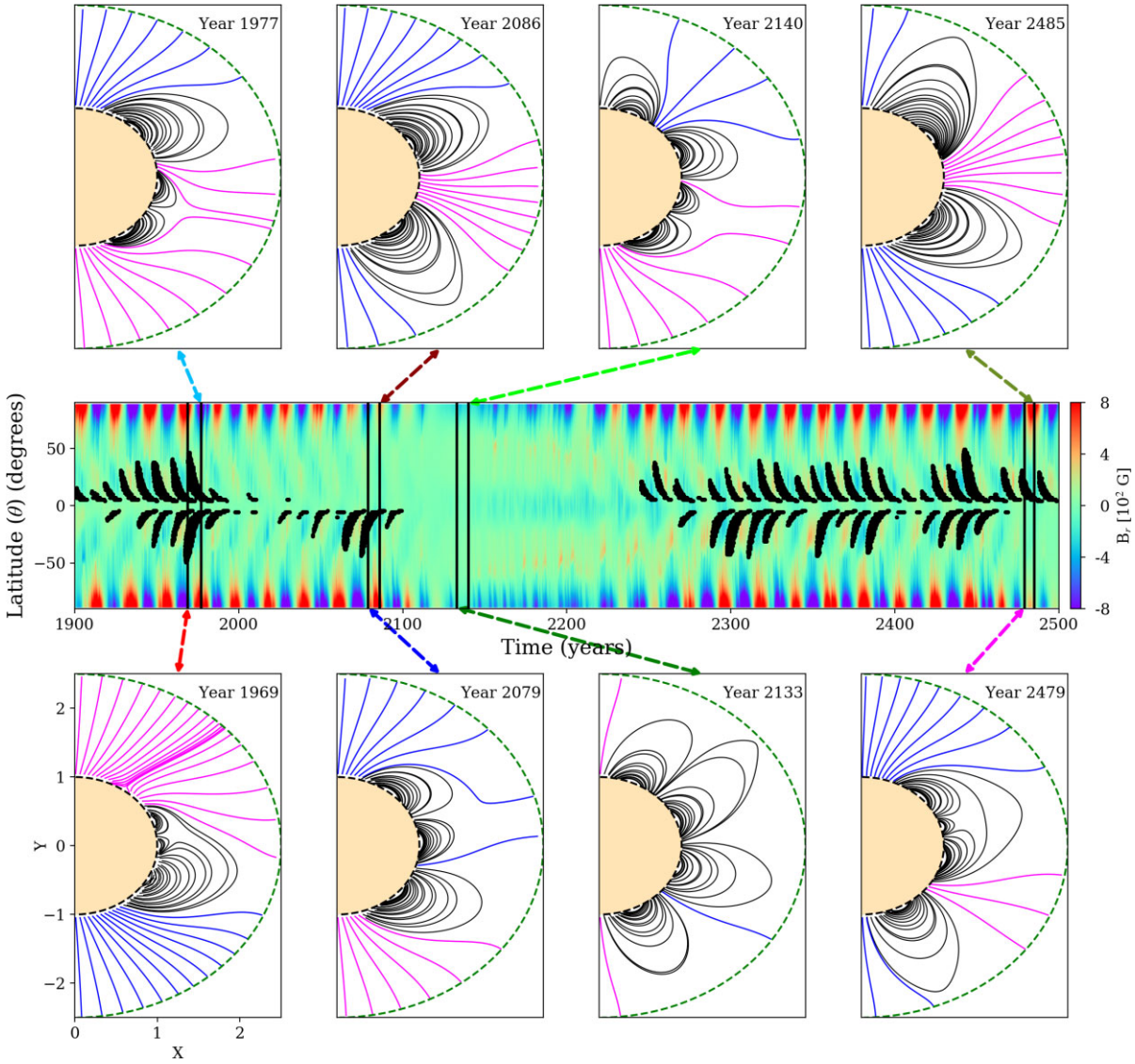

Figure 5. Solar coronal magnetic field configuration for different phases based on hemispheric sunspot eruptions. The butterfly diagram captures a time frame spanning over 600 years, starting from year 1900 until year 2500 with sunspot eruption proxies overplotted in black from the SURYA 2.5D kinematic solar dynamo model. The global solar coronal magnetic field configuration is plotted for different cases. The black curve denotes closed magnetic fields and the magenta/blue lines show radially inward/outward open field lines. Year 1969 and 1977 demonstrate a period where the sunspot eruptions are observed till high latitudes in both hemispheres in our simulation. For this case, the coronal magnetic field distribution indicates the presence of complex coronal loops closer to the equator. Year 2079 and 2086 denote a period where sunspot eruption proxies are absent only in the northern hemisphere. The resulting coronal magnetic field distribution shows a shift in parity (as the global dipolar structure is changed to a quadrupolar configuration in year 2086). For Year 2133 and 2140, sunspot eruption proxies are absent in both hemispheres. For this case, the extrapolated magnetic field distribution is quite complex. We notice closed magnetic field lines near polar high latitudes. We have assumed a fixed source surface height of $r = 2.5R_{\odot}$ for our modelling irrespective of the solar activity phase. Similarly, for a case where sunspot eruption proxies are absent in the southern hemisphere (Year 2479 and 2485), we observe complex coronal magnetic field structure along with a shift in parity in the large-scale solar magnetic field. The parity modulations result from the hemispheric decoupling and non-linear nature of the solar dynamo mechanism.

The evolution of radial magnetic field on the solar surface ($B_{\rm r}(R_{\odot})$) is shown in the butterfly diagram in the top panel of Fig. 1. The overplotted sunspot eruption proxies (plotted in black circles) denote the level of solar activity variation. In the butterfly diagram, the periods devoid of sunspot eruption proxies correspond to grand minima episodes. We find four such grand minima phases from Year 998 to 1139, Year 2099 to 2244, Year 3395 to 4098, and Year 4904 to 5119, where sunspot eruption proxies are absent in both the hemispheres. For such phases, the heliospheric modulation parameters e.g. OSF and the cosmic ray modulation potential show a dip (middle and bottom panel of Fig. 1). Additionally, there are several other instances of hemispheric grand minimum, where sunspot eruption proxies are absent in either one of the hemispheres.

In order to identify the grand minimum, regular activity, and grand maximum phases in our model output, we analyse the time series of sunspot eruption proxies. The mean value of the simulated SSN proxy time series is shown in the green-dashed line in the top panel of Fig. 2. We define a threshold of mean sunspot number + 3σ (red-dashed line in Fig. 2) to identify the grand maximum phases. For

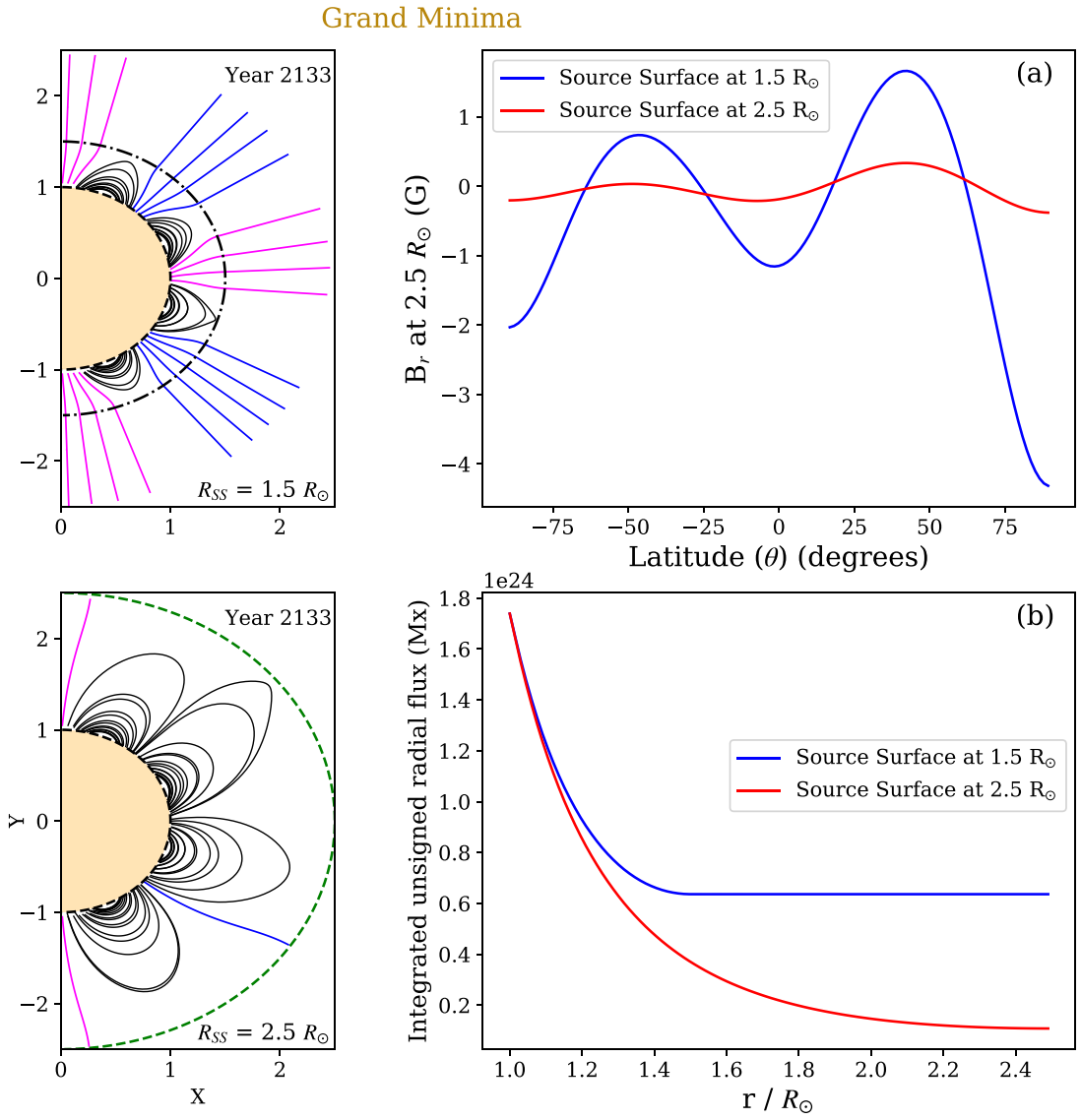

Figure 6. Coronal magnetic field distribution during a grand minima episode (year 2133) for two different source surface heights $r = 2.5R_\odot$ and $1.5R_\odot$. Green-dashed curve and black dash–dotted curve in the bottom panel identify the source surface height at $r = 2.5R_\odot$ and $1.5R_\odot$ in our model. (a) Extrapolated radial field (B_r) at $r = 2.5R_\odot$ as a function of latitude for $R_{SS} = 1.5R_\odot$ plotted in blue and for $R_{SS} = 2.5R_\odot$ plotted in red. (b) Variation of integrated unsigned radial flux at different heights when R_{SS} is at $1.5R_\odot$ (in blue) and $1.5R_\odot$ (in red). By lowering the source, surface closer to the surface, we observe more open field lines in the modelled output. However, the closed magnetic field lines still persist within the spherical source surface that may not have been captured in the historical total solar eclipse paintings. Source surface height is one of the key parameters for the calculation of OSF. Choosing a source surface distant from the surface during grand minimum phases results in a lower OSF value.

grand minimum phases, we identify the epochs in the time series, where there are no sunspot eruptions (at least for three consecutive cycles). Lastly, for the regular activity phases, the sunspot eruption proxy remains close to the global mean of the sunspot proxy (green-dashed line in Fig. 2). With this definition, we find multiple instances of grand maxima, grand minima, and regular activity phases in our simulation.

In the long-term reconstruction of the solar activity cycle over nine millennia, there are multiple occurrences of such fluctuating solar activity phases (Wu et al. 2018). This reconstruction provides a decadal averaged reconstructed SSN (see bottom panel of Fig. 2). Different components of the solar activity, i.e. grand maximum, grand minimum, and normal (moderate) phase, are identified in red, black, and green-dashed curves, respectively, in the bottom panel of Fig. 2. We analyse these different phases in terms of coronal magnetic field configuration.

3.1 Solar corona during grand maxima, grand minima, and a regular solar activity phase

The modulation of the state of the heliosphere by the solar coronal magnetic fields can be parametrized by OSF, which in turn impacts the cosmic ray modulation. OSF and the cosmic ray modulation potential are spatially averaged quantities. Hence, they lack a description of the solar coronal magnetic fields (whether they are open or closed within the solar source surface) that govern the flow of the solar wind in the heliosphere. In order to understand the spatial distribution of the fields during different solar activity

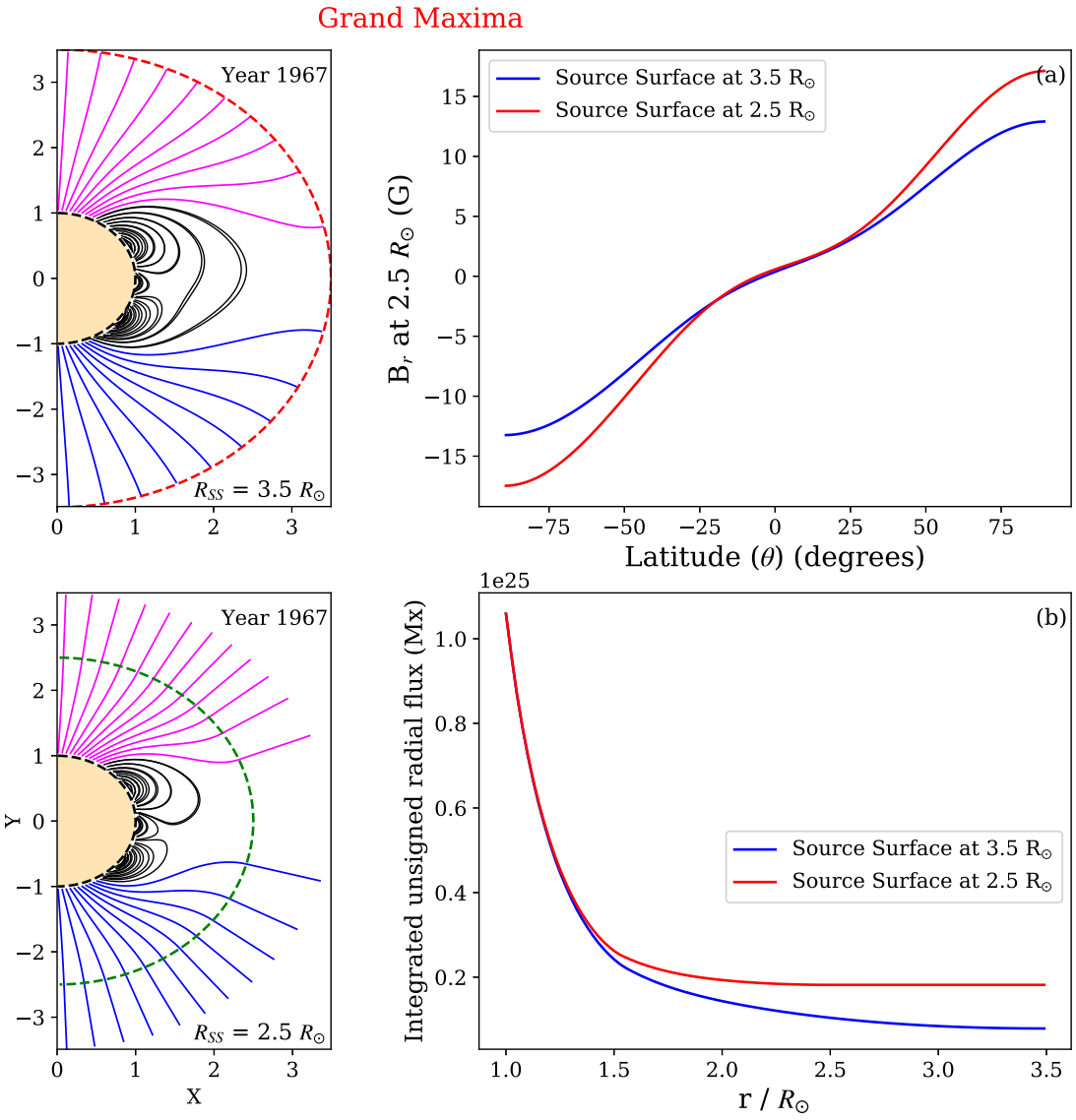

Figure 7. Distribution of magnetic field lines during a grand maxima episode (year 1967) for two different source surface heights $r = 3.5R_\odot$ and $2.5R_\odot$. The green/red-dashed curves in the plots show the source surface height at $r = 2.5R_\odot$ and $3.5R_\odot$. (a) Modelled radial field at $r = 2.5R_\odot$ as a function of latitude for $R_{SS} = 3.5R_\odot$ plotted in blue and for $R_{SS} = 2.5R_\odot$ plotted in red. (b) The integrated radial at different heights when R_{SS} is at $3.5R_\odot$ (in blue) and $2.5R_\odot$ (in red). Lowering of source surface height during a grand maximum phase results in the opening up of more field lines, which results in a higher radial field near the outer boundary and OSF value.

phases, we choose a grand maximum (from Year 1967 to 1979), grand minimum (from Year 2133 to 2145), and a regular activity phase (from Year 2296 to 2308) for further analysis. This choice of the solar activity phases is consistent with our definition based on the modelled sunspot eruption proxy time series. The coronal magnetic field configuration obtained using the PFSS model is provided in Fig. 3 for the corresponding years. Grand maxima, grand minima, and regular activity phases are denoted as shaded regions on the simulated $B_r(R_\odot)$ butterfly diagram in the bottom panel as (a), (b), and (c), respectively. For each of these episodes, the coronal magnetic field configuration is shown at a four-year time interval starting from the corresponding cycle minimum. We fix the source surface height at $r = 2.5R_\odot$ for consistency in our long-term simulation.

Near the cycle minimum in a grand maximum phase, we find the global corona to be in a dipolar state. We also find that the high-latitude regions are densely populated with open field lines (magenta for radially inward and blue for radially outward field lines), whereas the closed field lines are localized near the equatorial region (black for closed field lines), as shown in the panel (a), grand maxima phase of Fig. 3. For this phase, the global configuration of the corona shows a combination of closed and open field lines.

During the chosen grand minimum phase in our simulation, the sunspot eruption proxies are absent in both the hemispheres, indicating a reduced solar activity. The overall strength of the radial magnetic field is also significantly low as compared to other phases, which will be discussed later. The resulting coronal magnetic field configuration, as depicted in Fig. 3 (b), shows highly populated closed field regions in our model. We find the presence of these closed magnetic fields reaching high latitudes persisting throughout the grand minimum phase. Note that the variation of the source surface height during grand maximum and minimum can impact the coronal magnetic field configuration, as discussed in Section 3.3.

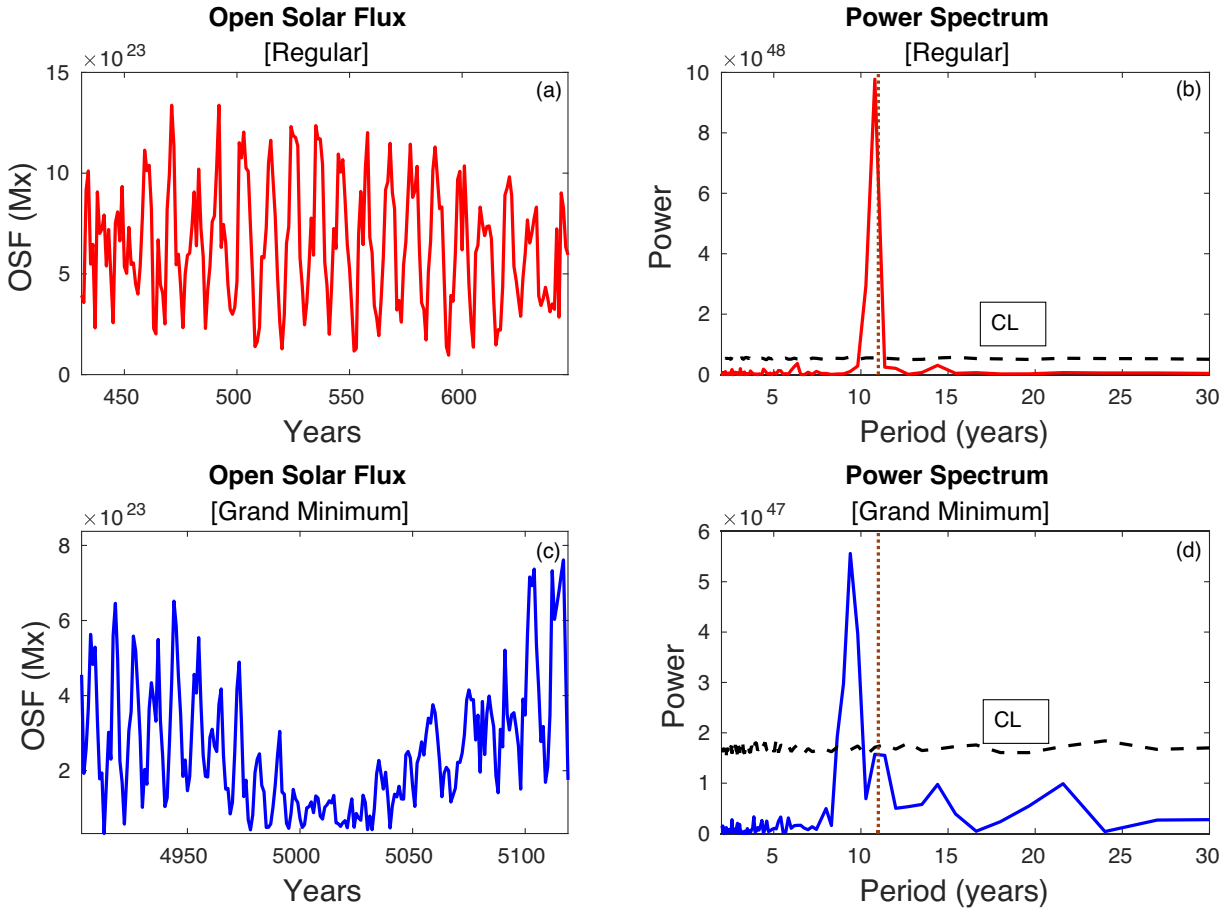

Figure 8. Spectral analysis on the simulated OSF time series. (a) The red curve indicates the time series of OSF for a regular activity phase (where there are finite sunspot eruption proxies on the solar surface) from year 432 to 648. (b) The red curve shows the power spectrum of OSF for the regular activity phase. FFT window size was chosen to be 1-year for our calculations. The overplotted black-dashed line denotes the upper 95th percentile of the FFT spectra for 1000 re-sampled OSF time series for the regular activity phase. (c) The blue curve shows the simulated OSF time series for one of the grand minimum episodes (year 4904 to 5120). (d) The power spectrum of OSF for the grand minimum phase. The black-dashed line here depicts the upper 95th percentile of the FFT spectra for 1000 re-sampled OSF time series. In panels (b) and (d), the brown dotted line in the FFT spectra denotes the 11-year cycle period for reference. The spectral power corresponding to the dominant period decreases during the grand minimum phase compared to the regular activity phase. We also observe a shift in the dominant period (shifts towards the lower period) during the grand minimum in our simulations. This behaviour is also present in the reconstructed OSF time series.

For a regular solar activity phase (Fig. 3 (c)), we observe the same polarity open field lines near both the poles at cycle minimum for Year 2296. This demonstrates the signatures of the quadrupolar parity in coronal magnetic fields. The global corona shifts to a dipolar parity after four years (Year 2300). In our solar dynamo model, we incorporate fluctuations in the poloidal source term for the Northern and Southern hemispheres independently. A combination of hemispheric decoupling due to stochastic fluctuations and non-linear terms in our model possibly contributes to parity modulation (see Hazra & Nandy (2019) for an extensive study focusing on this aspect). Independent studies by Beer, Tobias & Weiss (1998); Knobloch, Tobias & Weiss (1998) also find parity modulation due to co-existing interacting dynamo modes. During grand minima, regular activity, and grand maxima phases, the modulations in the coronal magnetic field configuration are caused by the variation in the surface magnetic field configuration.

The surface magnetic field distribution shapes the coronal magnetic fields, which in turn modulates the heliospheric parameters (e.g. OSF and cosmic ray modulation potential). In order to understand the variation of solar magnetic activity, we plot the variation of integrated unsigned radial flux with height for grand maxima (Year 1967), grand minima (Year 2133), and regular activity phase (Year 2296) in the top-right-hand panel of Fig. 4. The integrated unsigned radial flux is computed as $\int |B_r(r,\ \theta)| 2\pi r^2 \sin\theta\, \mathrm{d}\theta$ for different heights. Among these three different phases, the integrated unsigned radial flux is highest for the grand maximum and lowest during the grand minimum. The integrated unsigned radial flux for the regular phase lies between the grand maximum and grand minimum.

3.2 Solar coronal magnetic field configuration during cycle maximum and minimum phases

In Fig. 5, the coronal magnetic field configuration for different cases (based on the hemispheric appearance of sunspot eruption proxies) is presented at the corresponding cycle maximum and minimum. We choose a period from Year 1900 to 2500 for our analysis. Sunspot eruption proxies are denoted in dark circles over the butterfly diagram of the surface radial magnetic field, i.e. $B_r(R_\odot)$ in the middle panel of Fig. 5. For a phase, where the numbers of sunspot eruptions

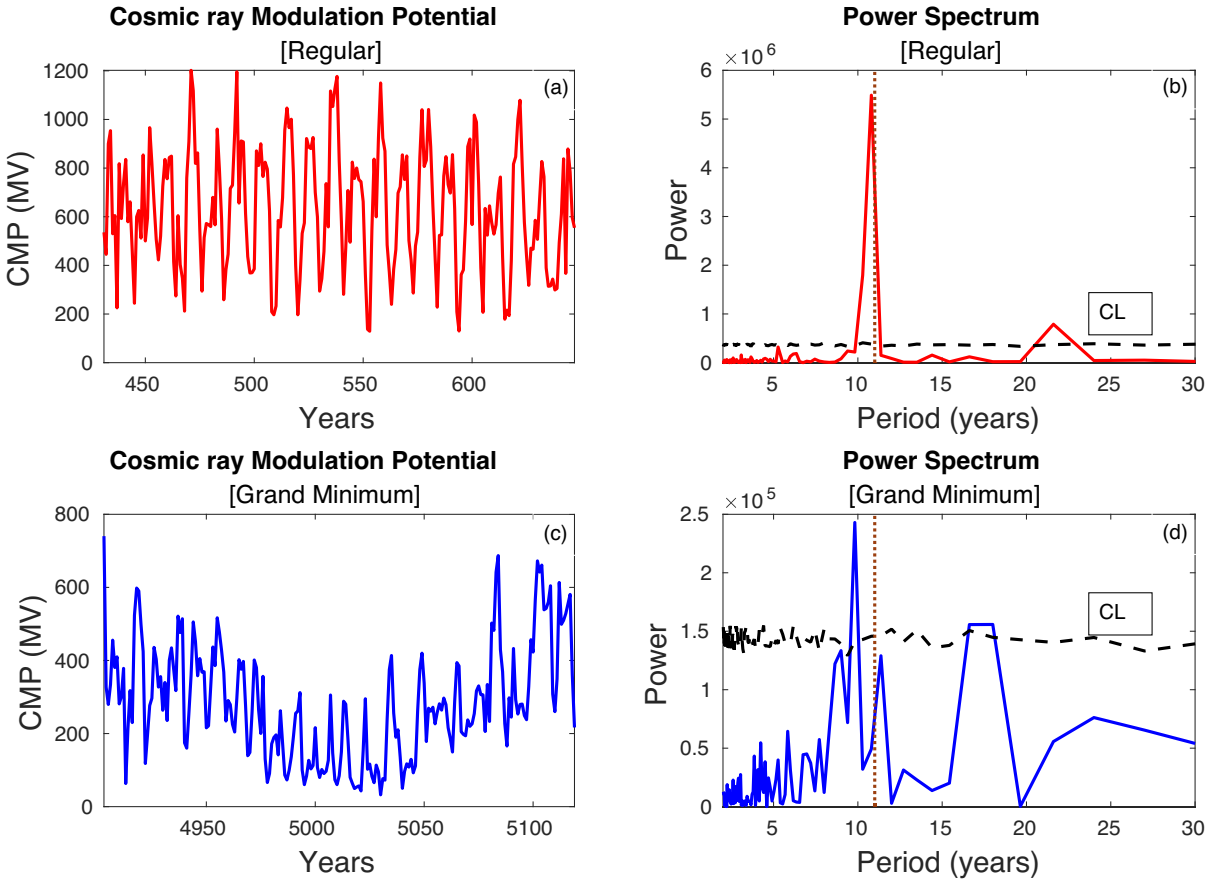

Figure 9. Spectral analysis of the simulated cosmic ray modulation potential time series. (a) The red curve shows the time series of cosmic ray modulation potential for a regular activity phase (where there are finite sunspot eruption proxies on the solar surface) from year 432 to 648. (b) The red curve shows the power spectrum of the time series. We have chosen the FFT window size to be 1-year for our calculations. The overplotted black-dashed curve denotes the upper 95th percentile of the FFT spectra of 1000 re-sampled cosmic ray modulation potential for the regular activity phase. This indicates the confidence level (CL). (c) The blue curve denotes the modelled modulation potential time series for one of the grand minimum episodes (year 4904 to 5120). (d) The power spectrum of the cosmic ray modulation potential for the grand minimum phase. The confidence level is plotted in the black-dashed line for this phase as well. 11-year periodicity is shown with a brown dotted curve on the FFT spectra. The power stored against the dominant period decreases during the grand minimum phase as compared to the regular phase.

are large in both hemispheres (close to a grand maximum phase), we find the eruptions reach a higher latitude compared to other phases. In such a phase (Year 1969), the coronal magnetic field configuration also shows a combination of closed and open field lines. The polarity of the polar fields is reversed at the end of the cycle (Year 1977), which can be seen in the polar coronal field lines. For a period where sunspot eruptions are absent only in the Northern hemisphere (Year 2079 and 2086), we find a shift in parity – from dipolar to quadrupolar – within the cycle. When the sunspot proxies are absent in both the hemispheres (Year 2133 and 2140), the global magnetic field configuration becomes complex. We find the presence of more closed fields near high-latitude regions for such phases. When the eruptions cease in the Southern hemisphere only (Year 2479 and 2485), we find the signature of parity modulation in the coronal magnetic fields. Such parity reversals in long-term solar dynamo simulations are reported by Hazra & Nandy (2019). The origin and impact of asynchronous solar activity across hemispheres have also been explored independently by Norton, Charbonneau & Passos (2014); Shukuya & Kusano (2017); Schüssler & Cameron (2018); Kitchatinov & Khlystova (2021).

3.3 Variation of source surface height during grand minima and grand maxima phases

The outer boundary of the PFSS model, i.e. the source surface is a spherical surface located at a constant height from the solar surface. At the source surface, the magnetic field is assumed to be purely radial and within the source surface, the coronal field is current free. In most studies, the value of source surface height ($r = 2.5R_{\odot}$) is fixed to match the observed interplanetary magnetic field pattern (Hoeksema et al. 1983). However, Schatten et al. (1969); Levine et al. (1977); Levine (1982); Lee et al. (2011) found that for low solar activity periods lowering the source surface height better matches the observations of open magnetic fields. Since our simulation covers periods of both grand maximum and minimum, we vary the source surface height in our simulation and explore the resulting changes in the coronal magnetic field configuration. Nevertheless, for the long-term computations, source surface is fixed at $R_{SS} = 2.5R_{\odot}$.

For the grand minimum phase, we do some additional extrapolation by setting the source surface height at $r = 1.5R_{\odot}$ and $2.5R_{\odot}$ in Fig. 6. The source surface heights are marked in the black dash–dotted curve for $r = 1.5R_{\odot}$ and in the green-dashed curve, $r = 2.5R_{\odot}$.

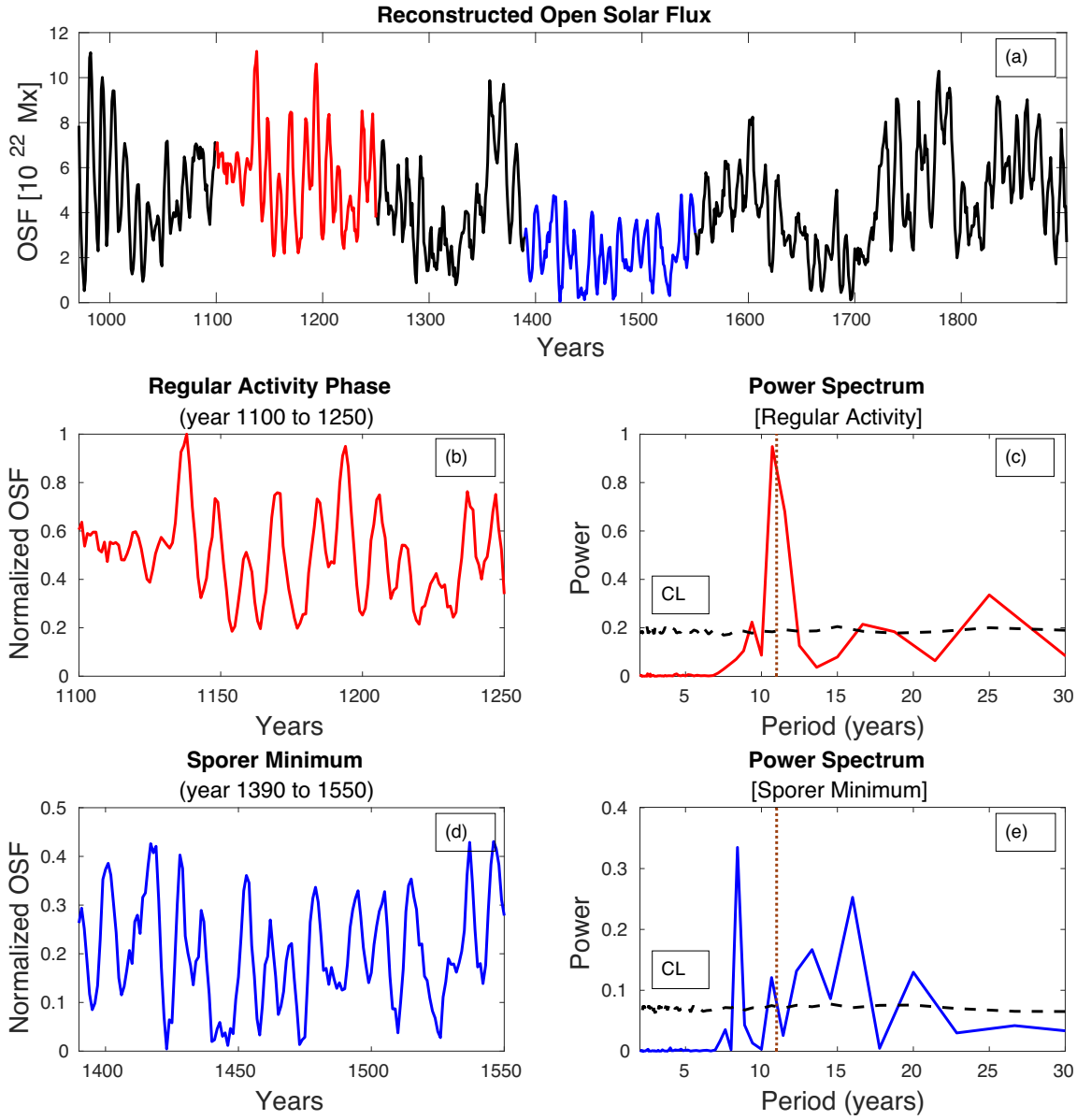

Figure 10. Fourier analysis of the reconstructed OSF. Reconstructed OSF data is obtained from Usoskin et al. (2021). (a) The time series of the OSF from year 971 to 1899 is shown in the solid black curve with the red-coloured region showing a regular activity phase (from year 1100 to 1250) and the blue-coloured region – spanning from year 1390 to 1550 – the Spörer minimum (one of the observed grand minimum episodes). (b) Normalized OSF for the regular activity phase is shown in the solid red curve. (c) The power spectrum of the regular activity phase is denoted by the solid red curve. Here, the brown dotted line denotes an 11-year period for reference. (d) Normalized OSF for Spörer minimum phase is plotted in the solid blue curve. Fourier power spectrum corresponding to the Spörer minimum phase is shown in panel (e). The solid black curve in panels (c) and (e) depicts the upper 95th percentile of the FFT spectra for 1000 re-sampled OSF time series. This determines the confidence level (CL). The power stored in the dominant cycle period decreases significantly during the grand minimum phase as compared to the regular activity phase. We find a similar trend in our modelled OSF as well.

We find the presence of open magnetic fields at a lower source surface height. However, the low-lying closed magnetic fields are persistent in this case as well. We also show the extrapolated radial magnetic fields at $r = 2.5R_\odot$ for both cases (see Fig. 6 (a)). It is to be noted that varying the source surface height, which is an unconstrained parameter (set to $2.5\,R_\odot$ for the whole simulation duration), may lead to a change in magnetic fieldline connectivity at a global coronal scale. Lowering the source surface height results in a higher radial field value during the grand minimum phase. For the integrated unsigned radial flux we find a similar trend as well (see Fig. 6 (b)). Similarly, for a grand maximum phase, we extrapolate the coronal magnetic fields for two different source surface heights $r = 3.5R_\odot$ and $2.5R_\odot$ (see Fig. 7). The source surface heights are shown in red and green-dashed curves here. Upon calculating the radial magnetic field at $r = 2.5R_\odot$ (see Fig. 7 (a)) and the integrated unsigned radial flux (see Fig. 7 (b)), we find a relatively higher flux near the boundary. In our long-term simulation, solar activity variations cover a wide range of activity episodes. Hence, for PFSS modelling, fixing the source surface height at $r = 2.5R_\odot$ can result in a higher OSF during the grand maximum phase and a lower OSF for the grand minimum phase.

3.4 Suppressed 11-year cycle period during grand minimum episodes

The evolution of heliospheric parameters, i.e. OSF and cosmic ray modulation potential, also follows the solar activity cycle. In order to explore the periodicities involved in the time series of OSF and cosmic ray modulation potential, we perform spectral analysis. Since there are multiple occurrences of grand minimum episodes in our long-term simulation, we choose the longest grand minimum phase for our analysis, which is from Year 4904 to 5120 (216 years). For comparison, we also selected a regular activity phase of the same length (from Year 432 to 648). We use the Fast Fourier Transform (FFT) with an annual cadence for deriving the power spectrum of OSF and cosmic ray modulation potential time series. Figs 8 and 9 show the time series and the power spectrum during a regular activity phase and a grand minimum phase for OSF and cosmic ray modulation potential, respectively.

In Fig. 8, for the power spectrum of simulated OSF, the dominant period during a regular phase is found to be 11 years (denoted by the brown-dashed curve in Fig. 8 (b)). However, for the grand minimum phase, we find a shift in the period towards a lower value with a significant reduction in power as compared to the regular phase (Fig. 8 (d)). For calculating the confidence levels, we randomize the sample 1000 times and perform FFT on each of the realizations. The upper 95th percentile for each period of these 1000 power spectra is defined as our confidence level (CL), which is denoted by the dashed-black curve for all the spectral analyses. For the simulated cosmic ray modulation potential, the power spectrum shows a dominant period of 11 years during the regular phase (Fig. 9 (b)). However, for a grand minimum phase, the dominant period again shifts towards a lower value with lower power than the regular phase (Fig. 9 (d)). The dominant peaks are identified by the CL curve on the power spectrum.

For comparison, we also computed the power spectrum using the observed 1000-year reconstructed OSF time series by Usoskin et al. (2021). The OSF is sampled at an annual cadence in this data set. For the grand minimum phase, we choose Spörer minimum (denoted by the blue colour in Fig. 10 (a) and (d)), which starts from year 1390 and ends at 1550. In order to compare with a regular phase, we choose a segment from year 1100 to 1250, which is a regular activity phase. Historical grand minimum time periods from the reconstructed data are reported in Usoskin et al. (2016). The power spectrum of the reconstructed OSF during the regular phase shows a dominant period of 11 years (Fig. 10 (c)). On the other hand, the power in the dominant period during the grand minimum phase is lower than in the regular phase. Therefore, the observations also show a similar shift in the power of the dominant period towards a lower value. This trend is independently confirmed by Saha, Chandra & Nandy (2022) who focused only on exploring the persistence of weak magnetic activity during grand minima phases. This demonstrates the qualitative consistency of spectral power distribution shifts in the observed OSF reconstruction and our long-term simulations.

4 CONCLUDING DISCUSSIONS

To summarize, we have simulated a 6000-year long solar activity time series covering grand maxima, grand minima, and regular activity phases utilizing a stochastically forced 2.5D kinematic solar dynamo model and potential field extrapolation technique. We also calculate the OSF and the cosmic ray modulation potential to understand the impact of solar activity on the state of the heliosphere. The stochastically forced dynamo results in the self-consistent generation of grand minima, maxima, and regular activity phases; these variations are manifested on the surface which governs the evolution of coronal magnetic fields and in turn modulates the heliospheric parameters e.g. OSF and cosmic ray modulation potential.

We find that the global configuration of the coronal magnetic fields changes during these different phases. The open flux that drives the solar wind into the interplanetary medium reduces during grand minima phases. We also find closed field regions distributed across all latitudes. When the height of the source surface in the PFSS model is lowered, these closed magnetic field lines persist very low down, close to the surface. Towards the end of the Maunder minimum (which is a grand minimum phase), a few solar eclipse paintings and simulations show a structure-less large-scale solar atmosphere (Riley et al. 2015; Hayakawa et al. 2021; Lockwood & Owens 2021). We surmise that less solar open field lines (and lower open flux) during grand minima phases – resulting from the surface field distribution governed by the solar dynamo output – culminates in a weaker driving of the solar wind. The cumulative effect of this is an overall enhancement in the cosmic ray flux arriving at the Earth during weak solar activity phases.

While explicit solar wind simulations are beyond the scope of this current paper, such fluctuations are reported in Owens, Lockwood & Riley (2017), where the authors reconstruct the solar wind for the past four centuries. In these reconstructions, the overall solar wind speed is indeed significantly reduced during the grand minimum phases and is higher during the regular phases. In this context, we point out the study by Pinto et al. (2011) who explore the physics of direct coupling between the dynamo and the solar wind. Understanding the physics of this coupling is essential to causally connecting dynamics from the solar interior to its atmosphere (Perri et al. 2018, 2020, 2021).

The source surface is expected to vary with solar activity levels. While a self-consistent treatment of this is only possible in dynamical models of coupled corona and interior, we have performed a few heuristic numerical experiments to study the impact of varying the local source surface in an ad hoc manner, which indeed has an impact on the structuring of the corona and the resultant open flux and cosmic ray modulation potential.

Cosmic ray flux is often used to reconstruct past solar activity. Reconstructions of past solar activity cycles based on cosmogenic isotope data encompass multiple occurrences of grand maxima, grand minima, and regular activity phases (Usoskin, Solanki, S. K. & Kovaltsov, G. A. 2007; Wu et al. 2018). Variations present in the reconstructed data are suggestive of fluctuations in the solar forcing. During grand minima phases, there is an observed reduction in the dominant power and a shift to a lower cycle period. Our long-term dynamo simulations covering diverse phases of solar activity are in qualitative agreement with this; another study focusing on solar cycle dynamics during grand minima phases lends independent support to these results (Saha et al. 2022).

In conclusion, based on a 6000 year kinematic dynamo simulation and potential field extrapolations of the coronal field forced by the dynamo generated magnetic fields, we find significant changes in the coronal structure and heliospheric forcing parameters, such as the open flux and cosmic ray modulation potential during distinct phases of solar activity. Our findings are qualitatively consistent with long-term reconstructions of solar open flux. Our study provides a theoretical basis for establishing causality between the solar dynamo mechanism and the long-term forcing of the state of the heliosphere. It also lays a firm foundation for the reconstruction of long-term (millennial scale) solar activity based on cosmogenic isotopes.

ACKNOWLEDGEMENTS

DN acknowledges fruitful exchanges at the Workshop on "Solar and Stellar Dynamos: A New Era" sponsored by the International Space Science Institute, Bern, where the idea of this work was initiated. The authors are thankful to Chitradeep Saha and Shaonwita Pal for helpful discussions. We acknowledge an anonymous referee for useful comments. SD acknowledges PhD fellowship from the DST-INSPIRE program of the Government of India. IU acknowledges partial support by the Academy of Finland (Project ESPERA No. 321882) and a visiting fellowship at ISSI (Bern). The Center of Excellence in Space Sciences India (CESSI) is funded by IISER Kolkata, Ministry of Education, Government of India.

DATA AVAILABILITY

We have used 1000-year OSF data available at VizieR online data catalogue (Usoskin et al. 2021). We have also used the decadal averaged reconstructed sunspot number data available at VizieR online data catalogue (Wu et al. 2018). Data from our simulations will be shared upon reasonable request to the corresponding author.

REFERENCES

Albert C., Ferriz-Mas A., Gaia F., Ulzega S., 2021, ApJ, 916, L9
Altschuler M. D., Newkirk G., 1969, Sol. Phys., 9, 131
Arden W. M., Norton A. A., Sun X., 2014, J. Geophys. Res. (Space Phys.), 119, 1476
Asvestari E., Usoskin I., 2016, J. Space Weather. Space Clim., 6, A15
Babcock H. W., 1961, ApJ, 133, 572
Badman S. T. et al., 2020, ApJS, 246, 23
Beer J., Tobias S., Weiss N., 1998, Sol. Phys., 181, 237
Bharati Das S., Basak A., Nandy D., Vaidya B., 2019, ApJ, 877, 80
Bhowmik P., Nandy D., 2018, Nature Commun., 9, 5209
Brehm N. et al., 2021, Nature Geosci., 14, 10
Cameron R., Schüssler M., 2015, Science, 347, 1333
Carbonell M., Oliver R., Ballester J. L., 1994, A&A, 290, 983
Charbonneau P., 2020, Living Rev. Sol. Phys., 17, 4
Chatterjee P., Nandy D., Choudhuri A. R., 2004, A&A, 427, 1019
Choudhuri A. R., Karak B. B., 2012, Phys. Rev. Lett., 109, 171103
Dash S., Bhowmik P., Athira B. S., Ghosh N., Nandy D., 2020, ApJ, 890, 37
Dasi-Espuig M., Solanki S. K., Krivova N. A., Cameron R., Peñuela T., 2010, A&A, 518, A7
Eddy J. A., 1988, Secular Solar and Geomagnetic Variations in the Last 10,000 Years, 1–23https://ui.adsabs.harvard.edu/abs/1988ssgv.conf....1E
Hayakawa H. et al., 2020, ApJ, 897, L10
Hayakawa H., Lockwood M., Owens M. J., Sôma M., Besser B. P., van Driel-Gesztelyi L., 2021, J. Space Weather. Space Clim., 11, 1
Hazra S., Nandy D., 2019, MNRAS, 489, 4329
Hazra S., Passos D., Nandy D., 2014, ApJ, 789, 5
Hazra S., Brun A. S., Nandy D., 2020, A&A, 642, A51
Hoeksema J. T., Wilcox J. M., Scherrer P. H., 1983, J. Geophys. Res., 88, 9910
Jouve L. et al., 2008, A&A, 483, 949
Kitchatinov L., Khlystova A., 2021, ApJ, 919, 36
Knobloch E., Tobias S. M., Weiss N. O., 1998, MNRAS, 297, 1123
Krivova N. A., Solanki S. K., Hofer B., Wu C. J., Usoskin I. G., Cameron R., 2021, A&A, 650, A70
Lee C. O., Luhmann J. G., Hoeksema J. T., Sun X., Arge C. N., de Pater I., 2011, Sol. Phys., 269, 367
Leighton R. B., 1969, ApJ, 156, 1
Levine R. H., 1982, Sol. Phys., 79, 203
Levine R. H., Altschuler M. D., Harvey J. W., Jackson B. V., 1977, ApJ, 215, 636
Lockwood M., Owens M. J., 2014, J. Geophys. Res. (Space Phys.), 119, 5193
Lockwood M., Owens M., 2021, Astron. Geophys., 62, 3
Muñoz-Jaramillo A., Nandy D., Martens P. C. H., Yeates A. R., 2010, ApJ, 720, L20
Nandy D., 2004, Sol. Phys., 224, 161
Nandy D., 2021, Sol. Phys., 296, 54
Nandy D., Choudhuri A. R., 2001, ApJ, 551, 576
Nandy D., Choudhuri A. R., 2002, Science, 296, 1671
Nandy D., Martens P. C. H., 2007, Adv. Space Res., 40, 891
Nandy D., Muñoz-Jaramillo A., Martens P. C. H., 2011, Nature, 471, 80
Nandy D., Bhowmik P., Yeates A. R., Panda S., Tarafder R., Dash S., 2018, ApJ, 853, 72
Nandy D., Martens P. C. H., Obridko V., Dash S., Georgieva K., 2021, Prog. Earth Planet. Sci., 8, 40
Norton A. A., Charbonneau P., Passos D., 2014, Space Sci. Rev., 186, 251
Owens M. J., Forsyth R. J., 2013, Living Rev. Sol. Phys., 10, 5
Owens M. J., Usoskin I., Lockwood M., 2012, Geophys. Res. Lett., 39, L19102
Owens M. J., Lockwood M., Riley P., 2017, Sci. Rep., 7, 41548
Passos D., Nandy D., Hazra S., Lopes I., 2014, A&A, 563, A18
Perri B., Brun A. S., Réville V., Strugarek A., 2018, J. Plasma Phys., 84, 765840501
Perri B., Brun A. S., Strugarek A., Réville V., 2020, J. Space Weather. Space Clim., 10, 55
Perri B., Brun A. S., Strugarek A., Réville V., 2021, ApJ, 910, 50
Pinto R. F., Brun A. S., Jouve L., Grappin R., 2011, ApJ, 737, 72
Potgieter M. S., 2013, Living Rev. Sol. Phys., 10, 3
Réville V. et al., 2020, ApJS, 246, 24
Riley P. et al., 2015, ApJ, 802, 105
Saha C., Chandra S., Nandy D., 2022, MNRAS, 517, L36
Schatten K. H., Wilcox J. M., Ness N. F., 1969, Sol. Phys., 6, 442
Schrijver C. J., De Rosa M. L., 2003, Sol. Phys., 212, 165
Schüssler M., Cameron R. H., 2018, A&A, 618, A89
Shukuya D., Kusano K., 2017, ApJ, 835, 84
Solanki S. K., Usoskin I. G., Kromer B., Schüssler M., Beer J., 2004, Nature, 431, 1084
Tripathi B., Nandy D., Banerjee S., 2021, MNRAS, 506, L50
Usoskin I., 2017, Living Rev. Sol. Phys., 14, 3
Usoskin I., Mursula K., Solanki S. K., Schüssler M., Kovaltsov G. A., 2002, J. Geophys. Res. (Space Phys.), 107, 1374
Usoskin I., Solanki S. K., Schüssler M., Mursula K., Alanko K., 2003, Phys. Rev. Lett., 91, 211101
Usoskin I., Alanko-Huotari K., Kovaltsov G. A., Mursula K., 2005, J. Geophys. Res. (Space Phys.), 110, A12108
Usoskin I., Solanki, S. K., Kovaltsov, G. A., 2007, A&A, 471, 301
Usoskin I. G., Gallet Y., Lopes F., Kovaltsov G. A., Hulot G., 2016, A&A, 587, A150
Usoskin I., Solanki S. K., Krivova N., Hofer B., Kovaltsov G. A., Wacker L., Brehm N., Kromer B., 2021, A&A, p. A141, 649
Wu C. J., Usoskin, I.G., Krivova N., Kovaltsov G. A., Baroni M., Bard E., Solanki S. K., 2018b, A&A, 615, A93
Yeates A. R., Mackay D. H., van Ballegooijen A. A., Constable J. A., 2010, J. Geophys. Res. (Space Phys.), 115, A09112

This paper has been typeset from a TEX/LATEX file prepared by the author.